Bioinspired Flapping-Wing Robot With Direct-Driven Piezoelectric Actuation and Its Takeoff Demonstration

Takashi Ozaki and Kanae Hamaguchi

***Abstract*—In this letter, we present the design and the performance of a prototype bioinspired flapping-wing micro aerial vehicle with piezoelectric direct-driven actuation. This type of actuation is superior in terms of structural simplicity because it does not include any transmission mechanism. Instead, a unimorph piezoelectric actuator directly drives the wing. We designed and fabricated a two-wing prototype with a wingspan of 114 mm and successfully demonstrated takeoff using an external power source under a one-degree-of-freedom constraint. The total mass of the prototype was 598 mg, and the maximum measured lift force was 6.52 mN (665 mgf) at a driving voltage of 100 V. We achieved tethered flight using the proposed direct-driven piezoelectric actuator considering the constraint.**

***Index Terms*—Piezoelectric actuators, biomimetics, mobile robots.**

I. Introduction

BIOINSPIRED flapping-wing micro aerial vehicles (FWMAVs) have received considerable attention given their potential for achieving the high maneuverability inherent to insects and birds within a lightweight and insect-sized structure. To manufacture such small FWMAVs, we must manage to develop a miniature actuation mechanism to produce the required reciprocal flapping motion in a wing.

Electromagnetic motors and piezoelectric actuators are the most successful actuation sources, and the former are prevalent in FWMAVs with weights above several grams. However, using motors for FWMAVs imposes a one-directional rotational motion. Thus, obtaining a reciprocal motion usually requires the addition of transmission mechanisms [1], [2]. For instance, AeroVironment, Inc. (Monrovia, CA, USA) designs transmission systems using gears, crankshaft, belts, and pulleys [2], with which they demonstrated a fully controllable flight of a hummingbird-mimetic robot with wingspan of 160 mm and weight of 19 g. In contrast, for smaller FWMAVs, piezoelectric actuation is considered the most promising technique given its high power density. In fact, a research group at Harvard University demonstrated the tethered flight of an insect-sized robot, RoboBee, using a piezoelectric bimorph actuator [3]–[5]. Still, a major challenge is the amplification of the small displacement produced by the piezoelectric effect. To this end, RoboBee uses a lever mechanism, whereas other studies have proposed amplification concepts using different materials and structures [6], [7].

Most designs combine an actuator and a motion-converting/amplification mechanism. In contrast, simpler mechanisms have been recently reported, in which transmission mechanisms are omitted, thus delivering direct-driving of the actuators on the wings [8]–[11]. Given that direct-driven actuation requires fewer components and stages of precision assembly, we consider that it could provide lower cost and higher reliability. We summarize some previous studies on direct-driving as follows. Hines *et al*. [8] proposed a simple flapping-wing actuation by connecting a wing to the shaft of a motor via a helical spring. By rotating the motor back and forth at the resonant frequency of the system, a large reciprocal flapping motion was generated along the wing with high power efficiency. Furthermore, they demonstrated tethered flight using a prototype with weight of 2.7 g, which is one of the lightest vehicles driven using a motor. Zhang *et al*. [9] optimized the resonant design and demonstrated liftoff using vehicles with weights ranging from 7.5 to 12 g and additional payload of 3.6 g. Regarding piezoelectric actuation, a research group at the US Army Research Laboratory developed a direct-driven piezoelectric flapping wing actuator, where the wing was directly connected to the piezoelectric bending actuator without using any transmission mechanism bending actuator without using any transmission mechanism [10]. The developers reported a large stroke amplitude (44° peak-to-peak) achieved by the very thin flexible unimorph actuator fabricated using a semiconductor process and resonant amplification. However, they did not demonstrate lift-force generation. Based on this concept, we previously reported an actuator that produces a lift force 1.9 times greater than its own weight [11]. However, our previous study did not include the flight demonstration of this mechanism.

In this study, we designed and fabricated a two-wing prototype FWMAV with a piezoelectric direct-driving mechanism and evaluated its performance. In addition, we successfully conducted a one-degree-of-freedom (1-DoF) takeoff using the prototype.

Manuscript received May 7, 2018; accepted July 30, 2018. Date of publication August 3, 2018; date of current version August 20, 2018. This letter was recommended for publication by Associate Editor B. Mazzolai and Editor Y. Sun upon evaluation of the reviewers' comments. *(Corresponding author: Takashi Ozaki.)*

The authors are with the Frontier Research Domain, Toyota Central R&D Labs., Inc., Aichi 480-1192, Japan (e-mail: ozaki@mosk.tytlabs.co.jp; kanae@mosk.tytlabs.co.jp).

This letter has supplemental downloadable multimedia material available at http://ieeexplore.ieee.org, provided by the authors. The Supplementary Materials contain a video file showing the takeoff demonstration of the prototype robot described in Section III-C. This video file shows the takeoff demonstration of the prototype robot. It includes the source movie of Fig. 17 and a close-up image from another viewpoint. This material is 21 MB in size.

Digital Object Identifier 10.1109/LRA.2018.2863104

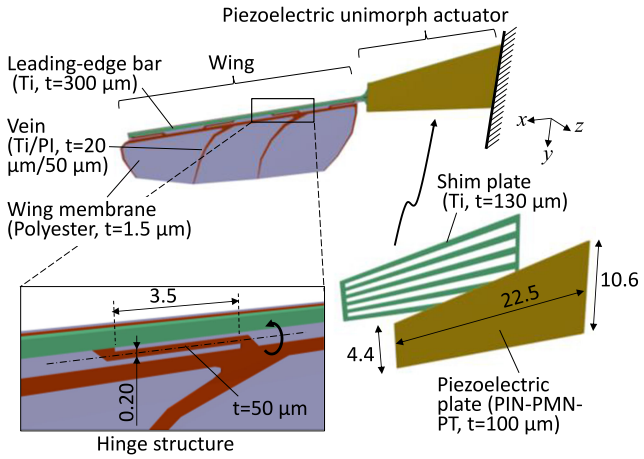

Fig. 1. Proposed direct-driven flapping-wing assembly. The zoomed hinge structure for pitch motion is shown at the bottom left. The shim plate has several slits that serve as pool for adhesive overflow.

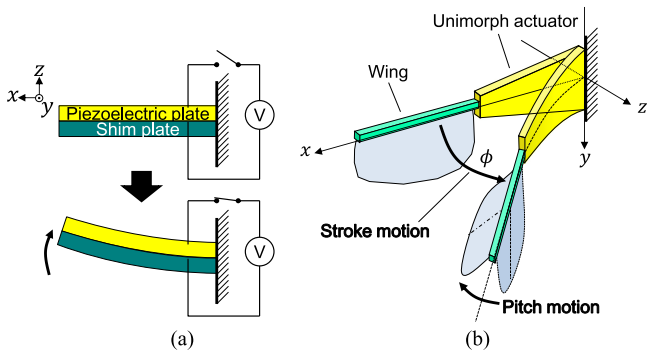

Fig. 2. Actuation principle: (a) behavior of unimorph actuator and (b) flapping motions of a wing attached to the actuator.

II. Design

A. Flapping-Wing Actuator

Fig. 1 shows the structure of the proposed direct-driven flapping wing. The assembly consists of only a wing and a trapezoidal piezoelectric unimorph actuator. The wing is composed of a Ti leading edge, a Ti/polyimide (PI) flexible vein, and a polyester membrane. A PI hinge structure is placed near the leading edge of the wing to realize pitch motion, which is crucial for generating lift force [12]–[14]. We employed $Pb(In_{1/2}Nb_{1/2})O_3$-$Pb(Mg_{1/3}Nb_{2/3})O_3$-$PbTiO_3$ (PIN-PMN-PT) as the piezoelectric material owing to its extremely high piezoelectric coefficient ($d_{32} = -1{,}156$ pm/V [15]) and relatively high elastic compliance ($s_{22}^{\mathrm{E}} = 69.97 \times 10^{-12}$ Pa^{-1} [15]), which enable large deformations. We fabricated the unimorph by attaching a 0.10-mm-thick PIN-PMN-PT plate onto a 0.13-mm-thick Ti shim plate with epoxy adhesive. We adopted the unimorph instead of the bimorph configuration by its simple assembling and wiring. Fig. 2 shows the operating principle of the actuator. When a voltage is applied to the piezoelectric plate, a strain is generated in it by the transverse piezoelectric effect, thereby bending the unimorph (Fig. 2(a)). This bending produces a stroke motion in the wing, as shown in Fig. 2(b). Moreover, a cyclic voltage at the resonant frequency of the actuator generates a large stroke amplitude. Along with the stroke motion, a pitch motion is passively generated via the air pressure and inertial force acting on the wing. We designed the wing with length R_w of 32.4 mm and maximum chord length of 11.1 mm. The length (L_A), fixed-end width (w_r), and tip width (w_t) of the unimorph were 22.5, 10.6, and 4.4 mm, respectively. The total length of the actuator was 54.9 mm. The weight of the actuator, corresponding to the sum of the weights of the piezoelectric plate, shim plate, and wing, was 217 mg.

We can explain the choice of the piezoelectric material based on a simplified motion equation of the actuator and approximating the actuator as a 1-DoF system. In addition, we consider that the unimorph deforms quadratically, the wing rotates only about the axis, i.e., $(x, z) = (L_A/2, 0)$, and the pitching is assumed to be constant. The simplified motion equation can be written as

$$J\ddot{\phi} + B\dot{\phi}\left|\dot{\phi}\right| + K\phi = GV, \tag{1}$$

where J is the effective inertia of the system, B is an aerodynamic damping coefficient, K is the spring constant of the unimorph, G is a moment factor associated with the piezoelectric effect, ϕ is the wing stroke angle, and V is the applied voltage on the piezoelectric plate. For the proposed design, $J = 1.80 \times 10^{-8}$ kgm^2 and $B = 4.18 \times 10^{-9}$ Nms^2 (see the Appendix for their derivations). In addition, K is calculated by

$$K = \kappa \frac{w_r + w_t}{2L_A}, \tag{2}$$

where κ is the bending stiffness of the unimorph per unit width, i.e., $\kappa = E_s t_s[t_s^2/12 + (y_c + t_s/2)^2] + E_p t_p[t_p^2/12 + (y_c - t_p/2)^2]$, with E_s and E_p being the elastic moduli of the shim and piezoelectric plate, respectively, t_s and t_p the thicknesses of the shim and piezoelectric plate, respectively, y_c the neutral axis of the unimorph, i.e., $y_c = \frac{1}{2}\frac{E_p t_p^2 - E_s t_s^2}{E_p t_p + E_s t_s}$. Moment factor G is obtained by

$$G = \frac{1}{2}(w_r + w_t)\left(\frac{t_p}{2} - y_c\right) d_p E_p, \tag{3}$$

where d_p is the transverse piezoelectric coefficient (refer to the Appendix for more details on K and G). We approximate the resonant frequency to $\omega_r = \sqrt{K/J}$. Applying $V = V_{\mathrm{pp}}(\sin(\omega_r t) + 1)/2$, we calculated ϕ during resonant driving by solving (1) using numerical integration obtained from function odeint in SciPy. The dimension-related parameters of the proposed actuator are $t_s = 130\,\mu$m, $t_p = 100\,\mu$m, $w_r = 10.6$ mm, $w_t = 4.4$ mm, and $L_A = 22.5$ mm, and the material properties are $E_s = 50.4$ GPa, $\rho_s = 2{,}250$ kg/m^3, and $\rho_p = 8{,}000$ kg/m^3, where E_s and ρ_s are 50% of those of Ti given by the slits in the Ti shim plate. We calculated ω_r and ϕ by varying the elastic compliance of the piezoelectric plate, i.e., $s_p = 1/E_p$, from 10^{-11} to 10^{-10} Pa^{-1}, which covers typical values of $Pb(Zr,Ti)O_3$ (PZT) and PIN-PMN-PT, assuming that d_p/s_p is a constant of 16.5 C/m^2 (typical d_p/s_p of PZT ceramics ranges from 10 to 17 C/m^2 [16], and d_p/s_p of PIN-PMN-PT is 16.5 C/m^2 [15]).

Fig. 3 shows results from analyzing the proposed actuator. By increasing s_p, ω_r decreases, and the stroke amplitude increases (Figs. 3(a) and 3(b)). In the figure, the ranges of s_p of the typical PZT and PIN-PMN-PT are represented as the yellow shaded area and red dashed line, respectively. The predicted stroke amplitude of the PIN-PMN-PT is ±28°, which is approximately twice the amplitude of the PZT. Consequently, the stroke amplitude can be increased by choosing a piezoelectric material with high s_p (i.e., low stiffness). The velocity of the wing is an important factor for the lift force as it depends on the square of

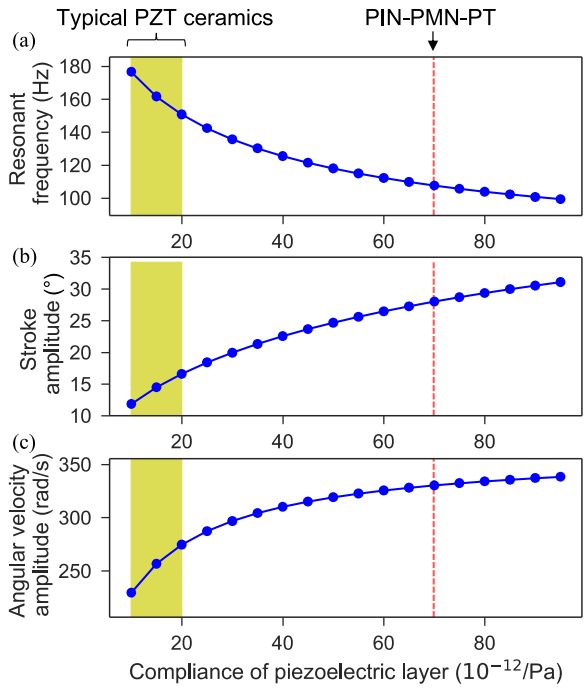

Fig. 3. Analysis of simplified model of flapping-wing actuator ($V_{\mathrm{pp}} = 100$ V).

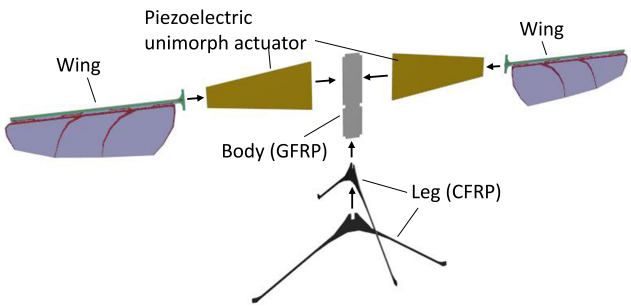

Fig. 4. Two-wing robot assembly.

the velocity. Fig. 3(c) shows that the angular velocity increases with the increase in s_p. From these results, we concluded that PIN-PMN-PT is more suitable for the direct-driven actuator.

B. Two-Wing Prototype

We designed and fabricated a prototype robot with two wings, as shown in Fig. 4. The piezoelectric actuators were attached to a glass fiber-reinforced plastic (GFRP) body with a thickness of 0.40 mm. In addition, four legs made of a carbon fiber-reinforced plastic (CFRP) plate with a thickness of 0.25 mm were bonded to the bottom of the GFRP body. No power sources or electrical circuits were mounted on the prototype, but the driving voltage was externally supplied via a thin flexible printed circuit (FPC) cable (not shown in Fig. 4) with a 12.5-μm-thick PI layer and 18 μm-thick copper lines without overlay. All the parts were assembled using a UV-curable adhesive (Loctite 4305; Henkel AG & Company, Düsseldorf, Germany). The weight of the prototype including the wings, unimorph actuators, body, and legs was 540 mg.

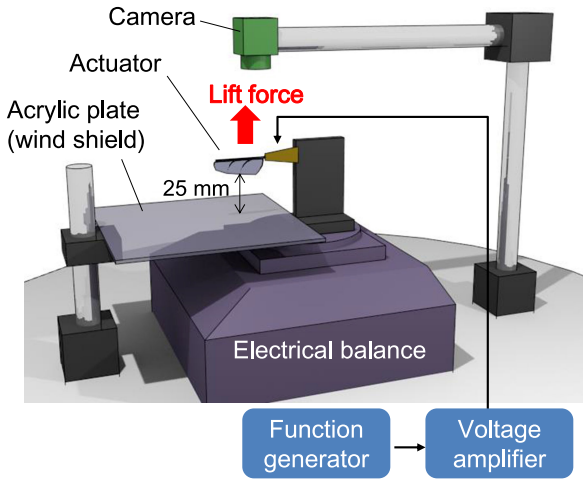

Fig. 5. Measurement setup for single actuator (not to scale).

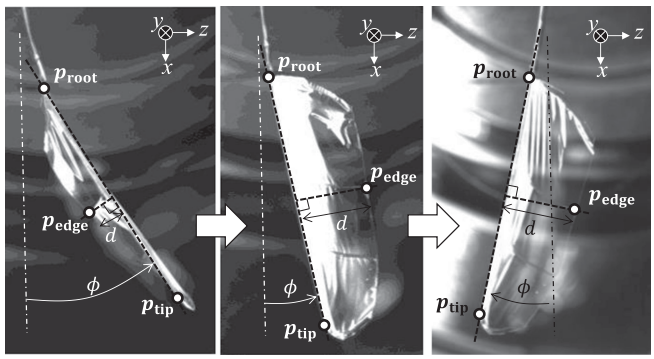

Fig. 6. Typical images of wing and tracked points for stroke and pitch angle analyses.

III. Results

A. Performance of Single Actuator

First, we measured the performance of a single flapping-wing actuator, which was rigidly fixed to a base. Fig. 5 shows the measurement setup used in this experiment. The average lift force was measured using an electric balance (HR-100A; A&D Co., Ltd., Tokyo, Japan) with force resolution of 0.1 mgf, linearity of $\pm$0.2 mgf, and averaging time of 4 s. The wing motion was captured using a camera (STC-CMB200PCL; OMRON SENTECH Co., Ltd., Kanagawa, Japan). Fig. 6 shows three typical captured images of the wing for angle estimation. We tracked three points on the wing: root $\boldsymbol{p}_{\mathbf{root}}$, tip $\boldsymbol{p}_{\mathbf{tip}}$, and center of the lower edge $\boldsymbol{p}_{\mathbf{edge}}$. Stroke angle ϕ was defined as the angle between the x axis and vector $\boldsymbol{p}_{\mathbf{tip}} - \boldsymbol{p}_{\mathbf{root}}$. Pitch angle ψ was calculated as $\psi = \arcsin(d/c)$, where c is the chord length and d is the distance between segments $\boldsymbol{p}_{\mathbf{tip}} - \boldsymbol{p}_{\mathbf{root}}$ and $\boldsymbol{p}_{\mathbf{edge}}$. To shield the balance from air motion generated by the wing, an acrylic plate was placed between the wing and the balance with a clearance between the wing lower edge and the plate of 25 mm. We applied the unipolar sinusoidal wave, $V_{\mathrm{pp}}\,(\sin(\omega_r t) + 1)/2$, as voltage signal to prevent the piezoelectric polarization from being inverted. Fig. 7 shows an image of the fabricated actuator with weight of 220 mg, which is close to the designed weight of 217 mg. The PIN-PMN-PT plate was manufactured by TRS Technologies, Inc. (State College, PA, USA).

Fig. 7. Image of the fabricated flapping wing assembly.

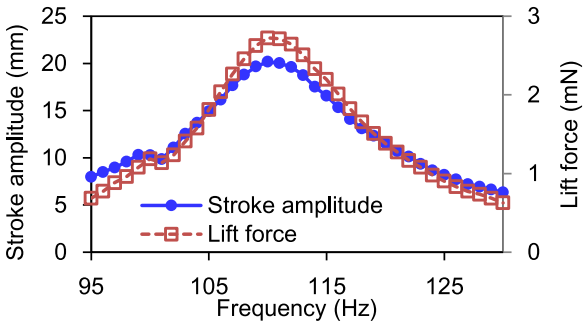

Fig. 8. Frequency response of single actuator ($V_{pp} = 60$ V).

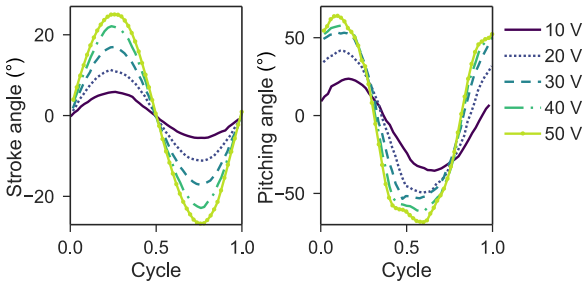

Fig. 9. Time variation of stroke and pitch angles.

First, to find the resonant frequency, we measured the frequency responses of the stroke amplitude and lift force, as shown in Fig. 8. The stroke displacement and lift force reach the maximum at a frequency of 110 Hz. Therefore, $\omega_r = 2\pi \times 100$ rad/s. This value is different to that reported by Zhang *et al.* [17], who obtained different peak frequencies given the relatively larger inertia of the wing compared to the aerodynamic damping. Based on their report, a frequency ω_p at the peak lift force can be calculated by solving the following system of equations:

$$\left.\begin{aligned} 2({B_2}^2 A^2 + J^2){\omega_p}^2 - 2JK = 0, \\ {B_2}^2 {\omega_p}^4 A^4 - (3K^2 - J^2 {\omega_p}^4 - 2JK{\omega_p}^2)A^2 \\ +3(KV_{pp}/2)^2 = 0 \end{aligned}\right\} \quad (4)$$

where A is the stroke amplitude and $B_2 = [8/(3\pi)]B$. When the wing inertia is much larger than the damping, i.e., $J >> B_2 A$, ω_p approaches ω_r. In fact, we confirmed that the difference between the calculated ω_r and frequency ω_p of our proposed actuator is less than 1 Hz (106.8 and 107.5 Hz, respectively). Next, we measured the motion and lift characteristics while varying V_{pp} in the range of 20–100 V at the resonant frequency of 110 Hz. We registered the displayed force once the value stabilized after approximately 5 s.

Fig. 9 shows the time variation of the stroke and pitch angles. The maximum stroke and pitch angles were 25.9° and 66.2°, respectively. Compared to insects or hummingbirds, the actuator has lower stroke amplitude and higher flapping frequency (the typical stroke amplitude and flapping frequency of hummingbirds with a size similar to our prototype are approximately 54° and 41 Hz, respectively [18]), whereas the pitch amplitudes are comparable. Fig. 10 shows the measured lift force according to the voltage amplitude from three samples fabricated using the same design. At $V_{pp} = 100$ V, the maximum average lift force of 4.79 mN (489 mgf) is obtained, with a max–min variation of 0.58 mN corresponding to 12.3% of the average. The average power consumption was 64.3 mW and the thrust-to-power ratio was 7.60 gf/W under this condition and measured using a power analyzer (PA1000; Tektronix, Inc., Beaverton, OR, USA).

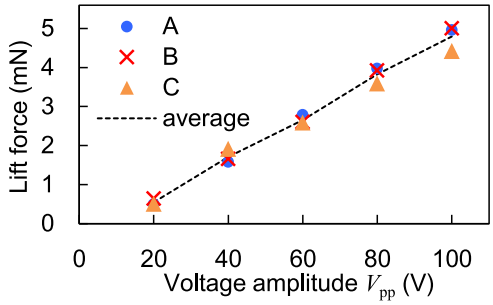

Fig. 10. Lift force according to voltage amplitude. Data from three samples, A, B, C, and average value, where sample A is that shown in Figs. 6–9.

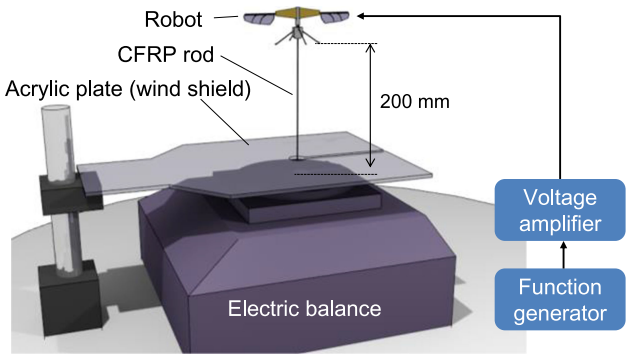

Fig. 11. Lift force measurement for the two-wing robot (not to scale).

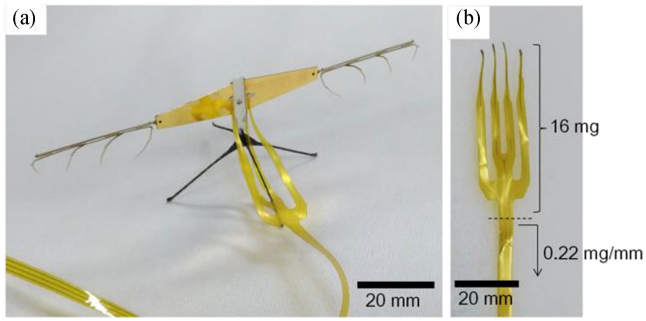

Fig. 12. Photographs of the (a) fabricated two-wing robot and (b) FPC cable.

B. *Performance of Two-Wing Prototype*

We evaluated the lift force of the prototype two-wing robot. Fig. 11 shows the measurement setup. The robot was fixed ontop of a CFRP rod with radius of 1.0 mm and length of 200 mm (the effect of the supporting condition on the resonance is explained in the Appendix). The lift force was measured using

TABLE I
MASS OF ROBOT AND ITS COMPONENTS

Component	Mass (mg)
Wings	66.0
Unimorph actuators	368
Body and legs	106
FPC cable	> 16
Assembled robot[a]	598

[a]Measured by loosely hanging the FPC cable connected to the voltage amplifier. Thus, this value includes a portion of the cable.

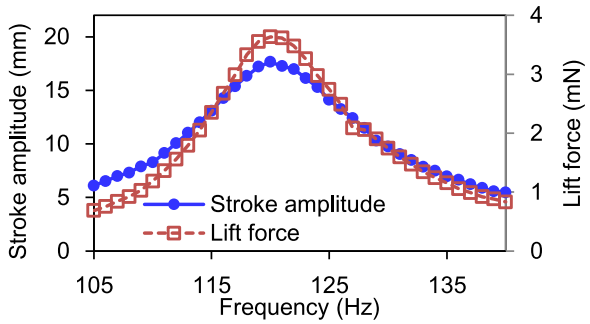

Fig. 13. Frequency response of the two-wing robot ($V_{pp} = 60$ V).

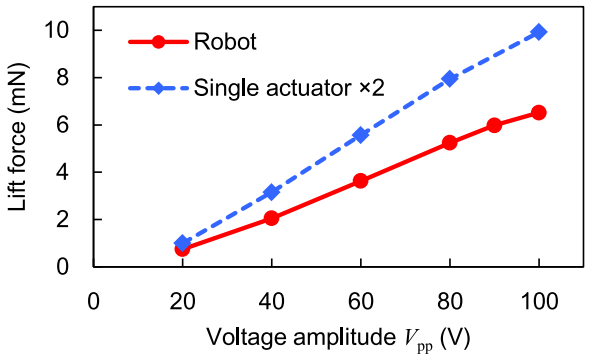

Fig. 14. Comparison among lift forces of doubled actuator and two-wing robot.

the electric balance. Fig. 12 shows the fabricated prototype and FPC cable, and Table I lists the masses of the robot components. Among the components, the unimorph actuator is the heaviest because it contains a large PIN-PMN-PT plate with high density (approximately 8,000 kg/m^3).

Fig. 13 shows the frequency response of the two-wing robot. The stroke displacement and lift force are maximum at a frequency of 120 Hz. Hence, the resonant frequency of the robot is approximately 10% higher than that of the rigidly fixed single actuator by the difference in fixing conditions. We employed a driving frequency of 120 Hz in the tests reported in the sequel. Fig. 14 shows the comparison of the doubled lift force from the rigidly fixed single actuator with the lift force from the two-wing robot placed on the flexible rod. The lift force of the robot corresponds to approximately 65% of the doubled force of the single actuator. This reduction cannot be explained by a variation in the actuator performance or the difference in the measurement configuration. For instance, it has been reported

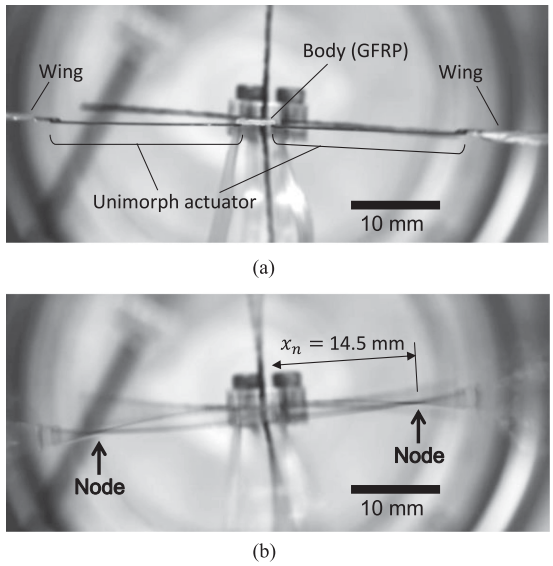

Fig. 15. Body and actuator oscillations at resonance: (a) before driving and (b) during resonant driving.

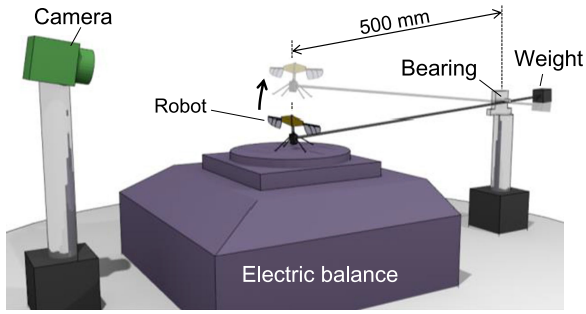

Fig. 16. Setup for take-off demonstration (not to scale).

that the clearance between the wing and the ground can vary the lift coefficient by up to 10% for the current setup [19], but this variation is much smaller that the measured reduction. We conclude that the reduction is mainly produced by the oscillation of the robot body. Fig. 15 shows top-view images of the robot during the measurements. Fig. 15(b) confirms that the body oscillates by the reaction force produced by the motion of the actuators and wings. The vibration node is found near the middle of the unimorph at a distance x_n of 14.5 mm from the root of the unimorph. Compared to the rigidly fixed actuator, the flapping span of the wing is lower for the same stroke angle. This difference makes the two-wing robot to produce a lift force lower than the doubled single-actuator force. This body oscillation can be related to the ratio of the body mass to the wing mass, as further explained in the next section. When $V_{pp} = 90$ V, the measured lift force was 5.98 mN (610 mgf), thus surpassing the weight of the robot and delivering a thrust-to-weight ratio of 1.1 for the prototype. Therefore, it can take off by applying a driving signal $V_{pp} \geq 90$ V.

C. Takeoff Demonstration

In this experiment, we demonstrated the takeoff of the two-wing robot under a 1-DoF constraint, as we are yet to implement altitude stabilization control. Fig. 16 shows the setup of the

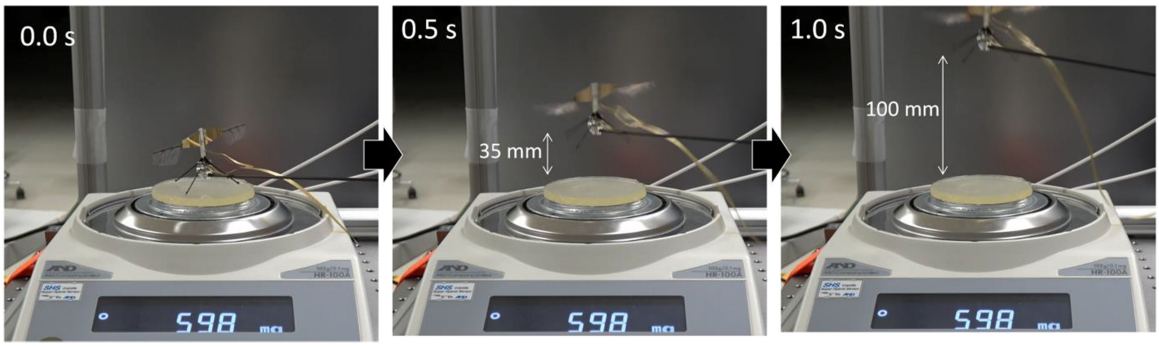

Fig. 17. Frames captured during takeoff of two-wing robot ($V_{\mathrm{pp}} = 90\,\mathrm{V}$).

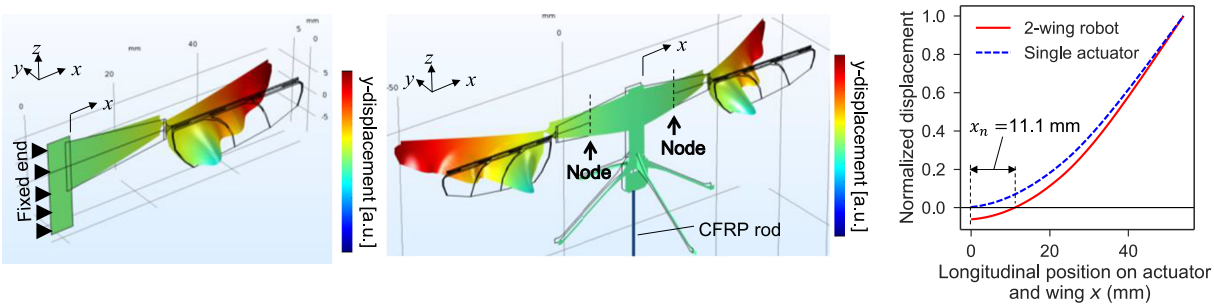

(a) (b) (c)

Fig. 18. Deformation shapes obtained using FEA under the resonant driving condition ($V_{\mathrm{pp}} = 100\,\mathrm{V}$): (a) fixed single actuator and (b) flexibly supported two-wing robot. (c) Actuator and wing deflections during resonant driving, where the x axis coincides with that shown in (a) and (b).

1-DoF constraint and related observations. The prototype was mounted on a seesaw structure (with arm length of 500 mm) that allows smooth rotation around a ball-bearing. We balanced the seesaw structure with a counterweight to cancel its mass but not that of the robot. With this setup, the angle variation due to arm rotation and the mass of the hanging FPC cable were expected to be the main sources of uncertainty for the lift force. Considering that the elevation height in this test is below 100 mm, the minimum force required for liftoff decreases by up to 2% because of the arm rotation, $1-\cos(100\,\mathrm{mm}/500\,\mathrm{mm})$. The linear density of the FPC cable was 0.22 mg/mm, and its variation range while hanging was approximately 22 mg, which is 3.7% of the total mass of the robot. We believe that these uncertainties are negligible for demonstrating the potential of the actuator as a lift-force generator. Fig. 17 shows the results of the experiment. At the beginning (0 s), the balance displayed 598 mg, which is equal to the measured mass of the prototype (Table I). When a driving voltage of $V_{\mathrm{pp}} = 90\,\mathrm{V}$ is applied, the prototype successfully takes off from the balance surface (after 0.5 s). As supplementary material, we included a movie file with the videoclips corresponding to Fig. 17 and close-up views. This material is available at http://ieeexplore.ieee.org.

IV. Discussion

As described in Section III, the lift force of the two-wing robot was below the doubled force of the rigidly fixed single actuator. In other words, the current configuration seems to be inefficient with respect to the thrust-to-weight ratio of the actuator. In this section, we discuss this point based on finite-element analysis (FEA), whose details are given in the Appendix. Figs. 18(a) and 18(b) show the results of the harmonic modal analysis for the resonant driving simulation. The geometrical displacement was simplified for the FEA using linearization, and the aerodynamic force was approximated as linear damping. The modal shape of the two-wing robot exhibits body oscillation similar to that observed in the experiment (Fig. 15(b)). Fig. 18(c) shows the y-axis displacement along the unimorph and wing during resonant driving. The vibration node position, x_n, of the two-wing robot supported by the CFRP rod was calculated to be 11.1 mm, which is comparable to the experimental result of 14.5 mm.

We considered two methods to suppress the body oscillation. The first method involves changing the mass (inertia) ratio of the body and wings by respectively increasing the body mass or decreasing the wing mass, thus affecting the body motion. Still, a very large additional mass is not feasible, and hence it should be below the recovered lift force. The second method involves designing the robot as a two-axis symmetric structure. For example, the robot could be given a four-wing configuration and x, y-axis symmetry by mirroring about the y axis, as shown in Fig. 18(b), where the reaction force of the wings should be canceled. In this study, we evaluated the first method by changing the mass ratio using FEA. Fig. 19(a) shows the calculated relationship between body mass and node position x_n, whereas Fig. 19(b) shows the relationship between the wing mass ratio to the proposed design and x_n. Both cases show a partial decrease of x_n. Thus, we confirmed that a lower wing/body mass (inertia) ratio effectively reduces the body oscillation. These results suggest that any or the combination of the variations allow to recover the lift force. The second method that employs a symmetric four-wing configuration should be also feasible. Therefore, we can employ these two methods for improving the proposed flapping-wing robot efficiency and behavior.

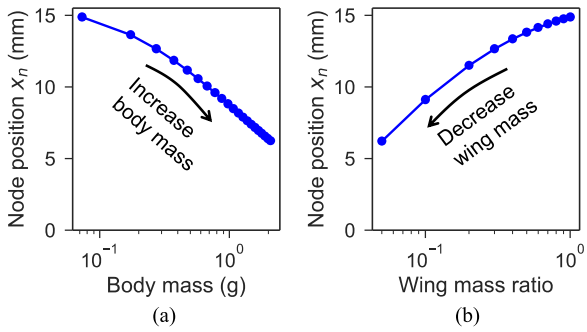

Fig. 19. Node position of the actuator at resonant vibration using FEA with varying (a) body mass and (b) wing mass ratio to the current design mass.

V. Conclusion

In this study, the liftoff of an FWMAV with direct-driven piezoelectric actuation was demonstrated. The maximum lift force and mass of the prototype robot were 6.52 mN (665 mgf) and 598 mg, respectively, and the maximum thrust-to-weight ratio was experimentally determined as 1.1. We believe that the simplicity of the proposed mechanism will enable the practical realization of FWMAVs, and we will engage in further developments. There are still some points to be considered regarding the superiority of the proposed mechanism. The cost of the piezoelectric material is one of them, as PIN-PMN-PT is currently more expensive than the prevalent materials such as PZT ceramics. In addition, the long-term reliability of the actuator is another concern because this mechanism requires a relatively large strain in the piezoelectric material.

To realize untethered flight, the lift force must be increased, as the current payload impedes holding a battery and a control circuit. Moreover, to achieve high maneuverability, additional lift force is required. Therefore, increasing the lift force represents an important design improvement. Likewise, the improvement should include the reduction of body oscillation. In addition, a system regulating torque is necessary for active altitude stabilization during free flight. Provided that the abovementioned symmetric four-wing configuration is employed, a control system similar to that used in drones may be suitable. Nevertheless, the evaluation of the resonance design on a robot with multiple actuators is needed to develop the stabilizing system. The mass distribution of the robot should be thoroughly considered, as the heavy actuators are placed away from the center, unlike the weight distribution found in insects and birds. These points will conform the basis of our future work.

Appendix

A. Simplified Parameters of Theoretical Model

We define J as the sum of inertias from the wing, J_w, and unimorph, J_A. We derived J_w using 3D CAD, obtaining $J_w = 1.55 \times 10^{-8}$ kgm^2, and estimated J_A from the kinematic energy of the unimorph, T_A. Assuming a quadratic deformation, the z-axis displacement of the unimorph, δ, is approximately $\delta \approx (1/2)(\phi/L_A)x^2$, and T_A is calculated as

$$T_A = \int_0^{L_A} \frac{1}{2}(\rho_s t_s + \rho_p t_p) w(x) \dot{\delta}^2 \mathrm{d}x, \tag{A1}$$

where ρ_s and ρ_p are the densities of the shim and piezoelectric plate, respectively, $w(x)$ is the width of the unimorph, $w(x) = w_r + (w_t - w_r)(x/L_A)$. J_A can be obtained from $J_A = (\partial T_A/\partial\dot{\phi})/\dot{\phi}$ as

$$J_A = \frac{1}{120}(\rho_s t_s + \rho_p t_p)(w_r + 5w_t){L_A}^3. \tag{A2}$$

As reported in [20], B is calculated as

$$B = \frac{1}{2}\rho_{\mathrm{Air}} C_D \int_{L_A/2}^{R_w + L_A/2} r^3 c(r) \mathrm{d}r, \tag{A3}$$

where ρ_{Air} is the density of air (1.29 kg/m^3), C_D is the drag coefficient, r is the distance from the wing root, and $c(r)$ is the chord length. Considering a constant angle of attack α, C_D was found to be 0.95 using from $C_D(\alpha) = 1.92 - 1.55\cos(2.04\alpha - 9.82)$ with $\alpha = 30^\circ$ [12]. K was calculated based on elastic energy U_A:

$$U_A = \int_0^{L_A} \frac{1}{2}\kappa w(x) \left(\frac{\partial\delta}{\partial x}\right)^2 \mathrm{d}x. \tag{A4}$$

Equation (2) was obtained from $K = (\partial U_A/\partial\phi)\phi$. The bending moment produced by the piezoelectric effect, M, is expressed as $M = E_p\, d_p\, w(x)(t_p/2 - y_c)V$. Thus, the static tip angle of the unimorph without load $\phi_{A,st}$ is calculated as

$$\phi_{A,st} = \int_0^{L_A} \frac{M}{\kappa w(x)}\mathrm{d}x = \frac{E_p d_p}{\kappa}\left(\frac{t_p}{2} - y_c\right) L_A V. \tag{A5}$$

The blocking moment of the unimorph was obtained using $K\phi_{A,st}$, and G was calculated using $K\phi_{A,st}/V$.

B. FEA Settings and Mesh Convergence

The linearized damping factor per unit area, D, that we employed for FEA is given by

$$D = \frac{1}{2}\rho_{\mathrm{Air}} C_N v_{\mathrm{ref}}, \tag{A6}$$

where C_N and v_{ref} are the perpendicular drag force coefficient and representative wing speed, respectively. We considered $C_N = 3.0$ and $v_{\mathrm{ref}} = 3.45$ m/s, which are typical values obtained from experiments. The structures in the actuator and two-wing robot were modeled using two-dimensional triangular shells, and the supporting CFRP rod was modeled as a one-dimensional beam element. The piezoelectric effect was simulated by bending moment M with $V_{\mathrm{pp}} = 50$ V in the shell element. We used COMSOL Multiphysics (Comsol, Inc., Burlington, MA, USA) for the FEA. To determine the mesh element size, we performed a mesh convergence study based on the eigen-frequencies using the model shown in Fig. 18(b), whose results are shown in Fig. 20, which depicts the relative errors of the eigen-frequencies up to the fifth mode. With the decrease in the average mesh size, the errors converge to zero. For average mesh size below 1.8 mm, the relative errors are lower than 0.1%. Hence, we considered that this was a suitable size for the FEAs.

C. Effect of Supporting Condition During Resonant Driving

We compared the deformation shapes of the robot in free state robot and supported by the CFRP rod (Fig. 11) during resonant

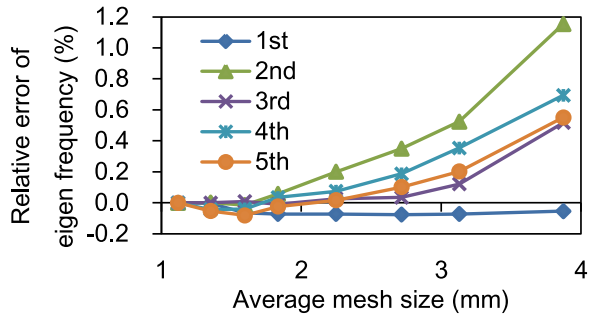

Fig. 20. Result of mesh convergence study. This graph shows the relative errors of the eigen frequencies with the smallest mesh size in the graph, i.e., 1.1 mm.

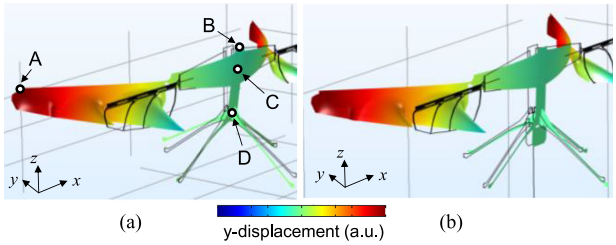

Fig. 21. FEA results of the robot in (a) free state and (b) supported by CFRP rod during resonant driving.

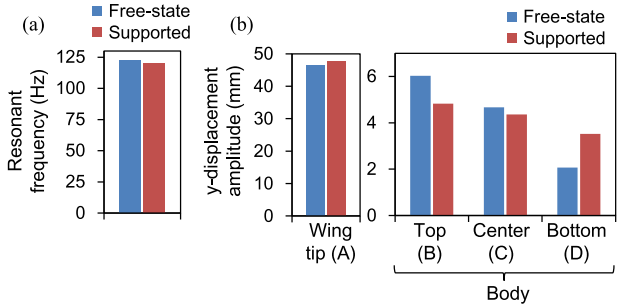

Fig. 22. (a) Resonant frequencies and (b) y-axis displacement of the free-state and supported robot obtained from FEA. Points A to D correspond to those shown in Fig. 21.

driving using the linearized FEA, whose results are shown in Fig. 21. The shapes of the free-state robot (Fig. 21(a)) and the supported robot (Fig. 21(b)) are very similar.

Fig. 22 summarizes the resonant frequencies and displacements at the wing tip and top/center/bottom of the body (indicated with letters A to D, respectively, in Fig. 21) for a detailed comparison. The resonant frequency, wing tip displacement, and body center displacement of the supported robot are almost equal to those of the free-state robot. The top and bottom body displacement of the free-state robot was greater than that of the supported robot. Therefore, the free-state robot exhibited a larger rotation around the x axis. However, the differences in the translational motions of the body were notably lower compared to the wing displacement. As the effects of the wing stroke amplitude and frequency on the lift force were dominant, we concluded that the effect of the supporting fixture on the measurement was negligible.

ACKNOWLEDGMENT

We would like to thank Editage (www.editage.jp) for English language editing.

REFERENCES

[1] G. C. H. E. de Croon, K. M. E. de Clercq, R. Ruijsink, B. Remes, and C. de Wagter, "Design, aerodynamics, and vision-based control of the DelFly," *Int. J. Micro Air Veh.*, vol. 1, no. 2, pp. 71–97, Jun. 2009.

[2] M. Keennon, K. Klingebiel, H. Won, and A. Andriukov, "Development of the nano hummingbird: A tailless flapping wing micro air vehicle," in *Proc. 50th AIAA Aerosp. Sci. Meeting Including New Horizons Forum Aerosp.*, Nashville, TN, USA, 2012, pp. 1–24.

[3] R. J. Wood, "The first takeoff of a biologically inspired at-scale robotic insect," *IEEE Trans. Robot.*, vol. 24, no. 2, pp. 341–347, Apr. 2008.

[4] K. Y. Ma, P. Chirarattananon, S. B. Fuller, and R. J. Wood, "Controlled flight of a biologically inspired, insect-scale robot," *Science*, vol. 340, no. 6132, pp. 603–607, May 2013.

[5] P. Chirarattananon, K. Y. Ma, and R. J. Wood, "Adaptive control of a millimeter-scale flapping-wing robot," *Bioinspiration Biomimetics*, vol. 9, no. 2, May 2014, Art. no. 025004.

[6] K. Mateti, R. A. Byrne-Dugan, S. A. Tadigadapa, and C. D. Rahn, "Wing rotation and lift in SUEX flapping wing mechanisms," *Smart Mater. Struct.*, vol. 22, no. 1, Dec. 2012, Art. no. 014006.

[7] V.-Q. Nguyen, M. Syaifuddin, H. C. Park, D. Y. Byun, N. S. Goo, and K. J. Yoon, "Characteristics of an insect-mimicking flapping system actuated by a unimorph piezoceramic actuator," *J. Intell. Mater. Syst. Struct.*, vol. 19, no. 10, pp. 1185–1193, Dec. 2007.

[8] L. Hines, D. Campolo, and M. Sitti, "Liftoff of a motor-driven, flapping-wing microaerial vehicle capable of resonance," *IEEE Trans. Robot.*, vol. 30, no. 1, pp. 220–232, Feb. 2014.

[9] J. Zhang, F. Fei, Z. Tu, and X. Deng, "Design optimization and system integration of robotic hummingbird," in *Proc. IEEE Int. Conf. Robot. Automat.*, Singapore, 2017, pp. 5422–5428.

[10] J. R. Bronson, J. S. Pulskamp, R. G. Polcawich, C. M. Kroninger, and E. D. Wetzel, "PZT MEMS actuated flapping wings for insect-inspired robotics," in *Proc. IEEE Int. Conf. Micro Electro Mech.*, Sorrento, Italy, Jan. 2009, pp. 1047–1050.

[11] T. Ozaki and K. Hamaguchi, "Performance of direct-driven flapping-wing actuator with piezoelectric single-crystal PIN-PMN-PT," *J. Micromech. Microeng.*, vol. 28, no. 2, Jan. 2008, Art. no. 025007.

[12] M. H. Dickinson, F.-O. Lehmann, and S. P. Sane, "Wing rotation and the aerodynamic basis of insect flight," *Science*, vol. 284, no. 5422, pp. 1954–1960, Jun. 1999.

[13] W. B. Dickson, A. D. Straw, and M. H. Dickinson, "Integrative model of Drosophila flight," *AIAA J.*, vol. 46, no. 9, pp. 2150–2164, Sep. 2008.

[14] M. R. A. Nabawy and W. J. Crowther, "On the quasi-steady aerodynamics of normal hovering flight part II: model implementation and evaluation," *J. R. Soc. Interface*, vol. 11, no 94, Feb. 2014, Art. no. 20131197.

[15] E. Sun, S. Zhang, J. Luo, T. R. Shrout, and W. Cao, "Elastic, dielectric, and piezoelectric constants of $Pb(In_{1/2}Nb_{1/2})O_3$–$Pb(Mg_{1/3}Nb_{2/3})O_3$–$PbTiO_3$ single crystal poled along $[011]_c$," *Appl. Phys. Lett.*, vol. 97, no. 3, Jul. 2010, Art. no. 032902.

[16] G. H. Haertling, "Ferroelectric ceramics: History and technology," *J. Amer. Ceramic Soc.*, vol. 82, no. 4, pp. 797–818, Apr. 1999.

[17] J. Zhang and X. Deng, "Resonance principle for the design of flapping wing micro air vehicles," *IEEE Trans. Robot.*, vol. 33, no. 1, pp. 183–197, Feb. 2017.

[18] B. W. Tobalske *et al.*, "Three-dimensional kinematics of hummingbird flight," *J. Exp. Biol.*, vol. 210, no. 13, pp. 2368–2382, Apr. 2007.

[19] H. Lu, K. B. Lua, Y. J. Lee, T. T. Lim, and K. S. Yeo, "Ground effect on the aerodynamics of three-dimensional hovering wings," *Bioinspiration Biomimetics*, vol. 11, no. 6, Oct. 2016, Art. no. 066003.

[20] T. Weis-Fogh, "Quick estimates of flight fitness in hovering animals, including novel mechanisms for lift production," *J. Exp. Biol.*, vol. 59, no. 1, pp. 169–230, Aug. 1973.